Geochemistry, Geophysics, Geosystems®

AGU ADVANCING EARTH AND SPACE SCIENCE

RESEARCH ARTICLE
10.1029/2021GC010265

Special Section:
Frontiers in lithospheric dynamics: bridging scales through observations, experiments, and computations

Geodynamic Modeling With Uncertain Initial Geometries

A. Spang[1], T. S. Baumann[1], and B. J. P. Kaus[1,2]

[1]Johannes Gutenberg University, Institute of Geosciences, Mainz, Germany, [2]TeMaS, Terrestrial Magmatic Systems Research Center, Mainz, Germany

Abstract Geodynamic codes have become fast and efficient enough to facilitate sensitivity analysis of rheological parameters. With sufficient data, they can even be inverted for. Yet, the geodynamic inverse problem is often regularized by assuming a constant geometry of the geological setting (e.g., shape, location and size of salt diapirs or magma bodies) or approximating irregular bodies with simple shapes like boxes, spheres or ellipsoids to reduce the parameter space. Here, we present a simple and intuitive method to parameterize complex 3D bodies and incorporate them into geodynamic inverse problems. The approach can automatically create an entire ensemble of initial geometries, enabling us to account for uncertainties in imaging data. Furthermore, it allows us to investigate the sensitivity of the model results to geometrical properties and facilitates inverting for them. We demonstrate the method with two examples. A salt diapir in an extending regime and free subduction of an oceanic plate under a continent. In both cases, small differences in the model's initial geometry lead to vastly different results. Be it the formation of faults or the velocity of plates. Using the salt diapir example, we demonstrate that, given an additional geophysical observation, we are able to invert for uncertain geometric properties. This highlights that geodynamic studies should investigate the sensitivity of their models to the initial geometry and include it in their inversion framework. We make our method available as part of the open-source software geomIO.

Plain Language Summary Computer models of geological settings have become a popular tool of research. They require the user to provide information on where the different geological units (rock layers, salt domes, magma bodies etc.) start and end as well as material parameters like density and strength of the units. As many of these input parameters are not well known, a lot of studies perform multiple simulations with different parameter combinations to investigate the influence the individual parameters and their uncertainties have. However, the initial geometry often remains fixed as it is difficult to describe with only few parameters and therefore unrealistic to vary. Here, we present a new method to describe and manipulate the geometry of geological units with a small number of parameters. This allows us to also vary the initial geometry and investigate how the model results depend on it. We apply our method to a salt diapir and a subduction zone to demonstrate the impact of initial geometry on the simulation results. To make our method available to the community, we implement it as a tool into geomIO, an open-source software package to generate initial geometries for geodynamic models.

Key Points:

- New, simple, intuitive and open-source method to describe and manipulate complex 3D bodies with a small number of parameters
- Allows for the integration of uncertainties of the initial geometry and enables inverting for geometric properties in numerical models
- Applications to a salt diapir with uncertain initial geometry and a subduction zone with uncertain initial subduction angle

Supporting Information:

Supporting Information may be found in the online version of this article.

Correspondence to:

A. Spang,
arspang@uni-mainz.de

Citation:

Spang, A., Baumann, T. S., & Kaus, B. J. P. (2022). Geodynamic modeling with uncertain initial geometries. *Geochemistry, Geophysics, Geosystems*, *23*, e2021GC010265. https://doi.org/10.1029/2021GC010265

Received 11 DEC 2021
Accepted 19 MAY 2022

Author Contributions:

Conceptualization: A. Spang
Data curation: A. Spang
Formal analysis: A. Spang
Funding acquisition: B. J. P. Kaus
Investigation: A. Spang
Methodology: A. Spang, T. S. Baumann
Project Administration: B. J. P. Kaus
Resources: B. J. P. Kaus

1. Introduction

Geodynamic modeling has become a powerful tool to investigate how different mechanical and thermodynamical parameters influence and control geological systems such as orogens, subduction zones, magmatic systems, basins, and other terrestrial bodies (e.g., Alisic et al., 2010; Baumann & Kaus, 2015; Jadamec et al., 2013; Ratnaswamy et al., 2015; Reuber et al., 2018). With the help of observations, the abovementioned studies can constrain rheology, density and thermal properties of geological units with forward and inverse approaches.

It is common practice in geodynamic modeling to assign material properties such as density and rheology in space with the help of geometrical objects that approximate units like rock layers, magma bodies or tectonic plates (van Zelst et al., 2021). There is a collection of open-source software packages covering this task. UWGeodynamics (Beucher et al., 2019, https://uwgeodynamics.readthedocs.io/) uses simple geometrical objects and polyhedra to generate setups for the Underworld code (Moresi et al., 2002, https://www.underworldcode.org/). GemPy (e.g., Varga et al., 2019; Schaaf et al., 2021, https://www.gempy.org/) allows the creation of layered and folded rock units, including faults and shapes like magma bodies and provides tools for gravity modeling and uncertainty analysis. The Geodynamic World Builder (Fraters et al., 2019, https://geodynamicworldbuilder.github.io/) focuses on ocean settings like subduction zones and spreading centers and is compatible with various

Software: A. Spang, T. S. Baumann
Supervision: T. S. Baumann, B. J. P. Kaus
Validation: A. Spang
Visualization: A. Spang, T. S. Baumann
Writing – original draft: A. Spang
Writing – review & editing: A. Spang, T. S. Baumann, B. J. P. Kaus

geodynamic codes. Tect_Mod3D (formerly SlabGenerator, e.g., Jadamec et al., 2013) is another software geared toward subduction zones. Easy (https://easyinit.readthedocs.io/) provides several tools to set initial conditions. geomIO (Bauville & Baumann, 2019, https://bitbucket.org/geomio/geomio) allows for the creation of 3D setups from vector graphic drawings (in Inkscape), provides gravity forward modeling and is coupled to the thermomechanical code LaMEM (Kaus et al., 2016).

Unlike the material properties themselves, the initial geometry of geodynamic models is usually treated as a constant throughout the study and not included in any parameter variations. This is because creating the initial geometry is, especially in three dimensions (3D), a time consuming process and parameterization is difficult (van Zelst et al., 2021). While the density of a geological unit can be described with a single number, defining its location and boundaries involves a large number of parameters if its shape is more complex than a basic geometric bodies such as planes, boxes, spheres or ellipsoids. Because of that, many modeling studies (e.g., Baumann et al., 2014; Čížková & Bina, 2015; Pearse & Fialko, 2010, and previously mentioned geodynamic studies) do not only have to ignore the uncertainties that are associated with the initial geometry but also lose the ability to investigate the influence of the initial geometry on the model results. Other studies generate different initial geometries and demonstrate a link between geometry and results, but can either not parameterize the geometry (e.g., Le Pourhiet et al., 2003) or are bound to simple properties like the thickness of a horizontal, planar layer (e.g., Duretz et al., 2020).

To facilitate the inclusion of a flexible geometry in geodynamic investigations, it needs to be efficiently parameterized with a number of geometrical parameters that does not outweigh the number of material parameters. Flexible geometries are commonly used in geomodeling (Wellmann & Caumon, 2018), potential-field modeling like gravity and magnetics (Jessell, 2001) and seismic inversion (Bosch et al., 2010). Techniques include voxel models (e.g., Guillen et al., 2004), discrete object modeling (e.g., Oldenburg & Pratt, 2007), flexible prisms (e.g., Fullagar et al., 2000), parameterized surfaces (e.g., Pereyra, 1996), explicit surfaces (e.g., Caumon et al., 2009) and implicit surfaces (e.g., Frank et al., 2007) but most approaches result in a collection of triangulated surfaces and/or voxel models (Galley et al., 2020).

It is our aim to present a method to intuitively parameterize and vary the 3D geometry of key features (e.g., salt domes, magma bodies, and subducting slabs) of geodynamic models. The method is implemented as a tool in geomIO (https://bitbucket.org/geomio/geomio) including a user manual and examples (https://bitbucket.org/geomio/geomio/wiki/VaryGeomTutorial.md) and is fully coupled to a state-of-the-art thermomechanical code in LaMEM (https://bitbucket.org/bkaus/lamem/src/master/). This facilitates the inclusion of geometric uncertainties in geodynamic modeling and enables us to constrain geometric properties of subsurface geological features with surface observations.

In Section 2, we present the method and show examples of how it works for arbitrary shapes and subducting plates. In Section 3, the method is applied to 2 different geological scenarios. (a) Seismic reflection reveals a salt diapir but its horizontal and vertical extent are uncertain. We generate an ensemble of possible initial geometries and demonstrate that they lead to distinctly different faulting patterns. This allows us to link geometric features to model results and constrain the geometry of the diapir with a synthetic surface observation. (b) We model free subduction of an oceanic plate underneath a continent and investigate the dependence of the velocities of both plates on the initial dip angle of the subducting slab. We also track the evolution of the dip angle as the plate subducts and compare the results to natural observations.

2. Methods

Our method is based on changing a single body at a time. As the definition of any complex 3D shape requires a large number of coordinates, we always need a reference model or starting geometry, which may be any 3D volume that is not a non-manifold geometry. We then create parameters which describe a transformation of this reference model into a different shape. Section 2.1 describes our general transformation algorithm applicable to any shape, and Section 2.2 shows an example of how it can be used to transform a sphere into a more complex shape. Section 2.3 shows how the method can be adapted for a subduction setting. Text S1 and Figure S1 in Supporting Information S1 explain the workflow of using the method in a geodynamic study.

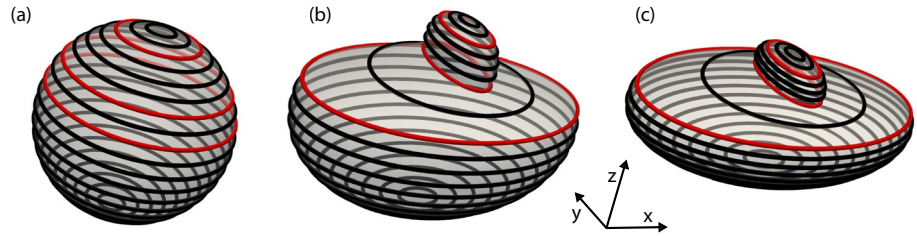

Figure 1. Illustration of 3D bodies as a set of 2D polygons. The three red slices are the control polygons which are used to transform the body. (a) Reference model sphere represented as horizontal polygons. (b) Sphere from 1a after transformation with the scaling parameters of Table 1. (c) Sphere from 1a after transformation with $Sz = 0.6$ and the scaling parameters of Table 1. Inset shows the orientation of the coordinate system.

2.1. Transformation Algorithm

2.1.1. Scaling Parameters

To manipulate the reference model, we compute the intersection of the 3D body with a finite number of horizontal planes that are perpendicular to the z-direction. In a second step, we select a subset of the resulting two-dimensional (2D) polygons (red in Figure 1a), which are referred to as control polygons. For each of the control polygons (P_i) we define two scaling parameters (Sx_i and Sy_i) and compute scaling parameters for all other polygons in the following manner:

1. Polygons below the lowermost control polygon copy its scaling parameters.
2. The scaling parameters of polygons between two control polygons are linearly interpolated between those of the control polygons.
3. Polygons above the uppermost control polygon copy its scaling parameters.

To achieve a homogeneous transformation in the horizontal plane, Sx_i must equal Sy_i which reduces the number of necessary parameters to one per control polygon. Finally, there is a single parameter (Sz) to transform the body in the vertical direction.

2.1.2. Vertical Scaling

To scale the body in the vertical direction, the spacing between the polygons is multiplied by the vertical scaling parameter (Sz):

$$z_{i,new} = (z_i - z_{ref}) * Sz + z_{ref} \tag{1}$$

where z_i is the vertical coordinate of the polygon and z_{ref} is the reference depth of vertical scaling. If $Sz > 1$, the body is vertically extended, if $Sz < 1$, the body is shrunk. z_{ref} should be chosen in dependence of the object to be transformed. For shapes like magma or ore bodies that are not bound to another unit, it makes sense to use the body's center of mass while for a salt diapir, its base is more appropriate.

2.1.3. Horizontal Scaling

To scale the body in the two horizontal directions, the following steps are applied to each polygon individually. First, we compute the position of the polygon's center of mass and transform the coordinates of all nodes on the polygon to be relative to it:

$$\left(\vec{x}_i' \; \vec{y}_i'\right) = \left(\vec{x}_i \quad \vec{y}_i\right) - \begin{pmatrix} x_{i_c} & y_{i_c} \\ \dots & \\ x_{i_c} & y_{i_c} \end{pmatrix} \tag{2}$$

Table 1
Scaling Parameters Used to Transform the Sphere in Figure 1a Into the Shapes in Figures 1b and 1c

Polygon	Sx	Sy
21	0.50	0.90
...	0.50	0.90
19	0.50	0.90
18	0.45	0.83
17	0.40	0.75
16	0.35	0.68
15	0.30	0.60
14	0.90	0.80
13	1.50	1.00
...	1.50	1.00
1	1.50	1.00

Note that the polygon numbering goes from the bottom to the top. Only the red numbers are free parameters that need to be chosen. The black numbers are generated automatically, depending on the red ones.

where $\vec{x}_i'$ and $\vec{y}_i'$ are vectors containing the relative coordinates of the nodes of the polygon, $\vec{x}_i$ and $\vec{y}_i$ are vectors containing the absolute coordinates of the nodes and x_{i_c} and y_{i_c} are the absolute coordinates of the polygon's center of mass. Then, all x-coordinates are multiplied by Sx_i and all y-coordinates by Sy_i. Lastly, the coordinates are transformed back into absolute values:

$$\left(\vec{x}_{i,new} \quad \vec{y}_{i,new}\right) = \left(\vec{x}_i' \quad \vec{y}_i'\right) * \begin{pmatrix} Sx_i & 0 \\ 0 & Sy_i \end{pmatrix} + \begin{pmatrix} x_{i_c} & y_{i_c} \\ \dots & \\ x_{i_c} & y_{i_c} \end{pmatrix} \tag{3}$$

If $Sx_i > 1$, the polygon extends in x-direction and if $Sx_i < 1$, the polygon shrinks. The same is true for Sy_i and the y-direction.

2.1.4. Additional Options

Equations 1–3 are the core of our method and sufficient to describe all operations used in the following example and the application in Section 3.1. Text S2 in Supporting Information S1 describes additional options that we implemented.

2.2. Example

For the sake of convenient visualization, we choose a sphere as our reference model. We represent the sphere with 21 equally spaced, horizontal polygons (Figure 1a) but the number of plain intersections is arbitrary. Polygons 13, 15, and 19 are chosen to be control polygons (red in Figure 1a) and for each one we set the parameters Sx and Sy (red in Table 1). The other scaling parameters are then computed according to Section 2.1.1 and used to transform the sphere in Figure 1a into the shape shown in Figure 1b. As we did not specify a vertical scaling parameter Sz, the body does not change its height. Figure 1c shows another example using the same parameters of Table 1 with $Sz = 0.6$.

The procedure can be imagined as pulling ($S > 1$) or pinching ($S < 1$) a rubber object at the locations of the control polygons. The only difference being, that the top and bottom of the object are not fixed but deform together with the closest control polygon. To keep top or bottom fixed, simply make the first (bottom) or last (top) polygon a control polygon with $S = 1$.

The number and position of the control polygons and the scaling parameters can be chosen by the user. Examples of using the tool are given at: https://bitbucket.org/geomio/geomio/wiki/VaryGeomTutorial.md.

2.3. Subduction Zones

Subduction zones are frequently investigated in geodynamic modeling studies. A central element is the orientation and location of the subducting slab. In this case, it is more convenient to represent the subducting plate as a collection of vertical polygons (Figure 2). We automatically detect the polygon nodes that make up the slab part (red in Figure 2b) and rotate them by angle θ to change the subduction angle (blue in Figure 2b). For 3D slabs that dip obliquely to the orientation of the coordinate system (Figure 2a), we first detect the direction of dip and recalculate θ' in the plane of the polygons so that the entire slab is rotated correctly. Additional rotation centers can also be placed anywhere along the slab to bend the deeper parts (Figure S5 in Supporting Information S1). This can be useful when the dip of the slab is well constrained close to the surface but changes at depth like along the west coast of South America.

Subduction setups often require a weak zone of elevated temperature, lowered viscosity or lowered yield strength to facilitate slip of the slab along the overriding plate. We automatically generate a weak zone of desired thickness following the curvature of the slab from the surface to a desired depth (green in Figure 2). Likewise, we can automatically add oceanic crust of desired thickness to the top of the slab (light blue in Figure 2).

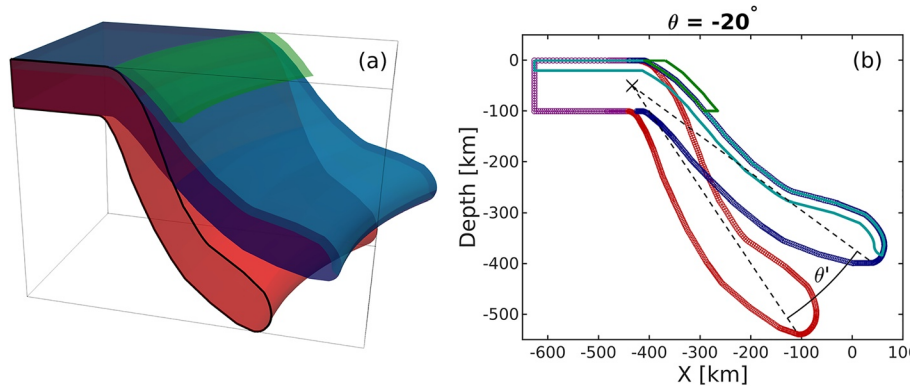

Figure 2. (a) 3D Example of a plate, subducting along a curved trench, drawn in geomIO (red) and an automatically generated variation with reduced subduction angle of 20° (blue). Alongside the variation, we can also automatically generate oceanic crust (light blue) and a weak zone (green) between slab and overriding plate. Black line shows one of the vertical polygons that the 3D volume is represented as inside our algorithm and is identical to the red + purple polygon in (b). (b) Representation of the plates in (a) as vertical polygons. Original in red, variation in blue, crust in light blue and weak zone in green. Purple nodes belong to both versions. Black cross shows the center of rotation.

3. Applications

In this section, we present two examples of applications to geological scenarios. Section 3.1 focuses on fault development associated with a salt diapir in an extending regime, including forward simulations and inversion. In Section 3.2, we investigate the dependence of plate velocity on the initial dip angle of a subducting plate and the evolution of the dip angle. Spang et al. (2021) presents a third application in 3D to a magmatic system.

3.1. Application I: Salt

Our method is especially useful when constraints from imaging studies are ambiguous like in the case of the Epsilon diapir in Norway (Jackson & Lewis, 2012). After a seismic survey, the stem of the diapir was interpreted to be about 300 m wide (green in Figure 3) but a drilling survey revealed it to be more than 1 km wide instead. Jackson and Lewis (2012) state that the location of the flanks can move hundreds of meters depending on the interpretation of the survey. The authors present a tear-drop-shaped post-drilling interpretation (dashed purple in Figure 3) of the diapir's extent but acknowledge that most of the margins are still uncertain. Jones and Davison (2014) revisit the data on the Epsilon diapir and present a much straighter interpretation (solid purple in Figure 3).

Here, we use the survey of the Epsilon diapir to show how different initial geometries, within the range of uncertainty of imaging data, can result in vastly different model results. We also demonstrate how geodynamic models with variable initial geometries, supported by other observations, can help reduce ambiguity of imaging studies. Figure 3 shows the reflection profile and various interpretations. Without the information of the drilling survey, the red outline could also be a valid interpretation, so we use it as an initial guess and reference model for our variations. The dashed yellow lines show the location of four control polygons located at the basis, the thinnest (neck) and thickest (head) part of the diapir as well as on the transition from neck to head.

3.1.1. Faulting Patterns in Dependence of Initial Geometry

Using the red outline in Figure 3 as an initial guess or reference model, we create about 1,500 different diapirs. For each variation, we generate a set of scaling parameters (S_1 to S_4) to be applied at the control polygons as well as one parameter (Sz) to vary the height of the diapir. Because it is a 2D example, S_1 to S_4 are equivalent to Sx_1 to Sx_4 and there are no Sy parameters. We generate the scaling parameters on a regular grid within the ranges given in Table S3 in Supporting Information S1 and add random noise to sample the parameter space. The reference depth for scaling in the vertical direction is the base of the diapir.

We then model the evolution of each diapir in an extensional geodynamic setting for 100 kyrs, using the thermomechanical code LaMEM (Kaus et al., 2016). We employ a linear-visco-elasto-plastic rheology and a density

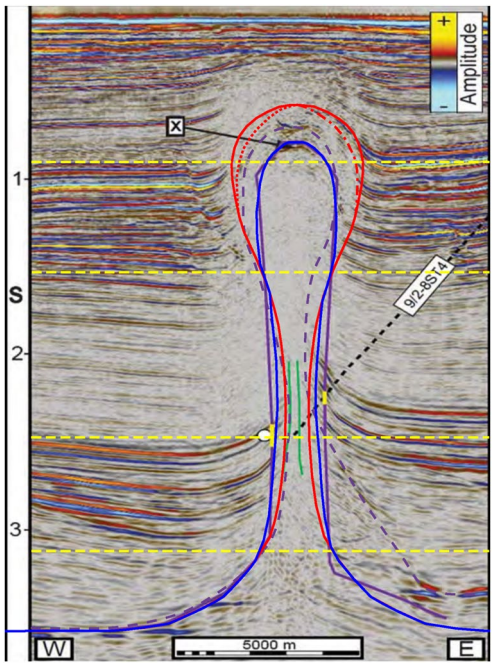

Figure 3. Seismic reflection profile of the Epsilon diapir modified from Jones and Davison (2014). Green lines show pre-drilling interpretation, dashed purple, post drilling interpretation of Jackson and Lewis (2012) and solid purple post-drilling interpretation of Jones and Davison (2014). Red line shows our symmetric initial guess and reference model. Dotted and dashed-dotted red lines show mirrored variations of red to test the effect of asymmetry. Solid blue line shows our synthetic "true" geometry that we try to fit in section Section 3.1.2. Dashed yellow lines show location of control polygons.

contrast of 500 kg m^{-3}. A more detailed description of the code and the material parameters can be found Text S3 in Supporting Information S1.

From the model output, we binarize the accumulated plastic strain to automatically identify faults that developed to accommodate the extension. With the help of principle component analysis, we extract preferred orientation (α), length (l), aspect ratio (r) and the location (x, z) of the faults or fault systems. The aspect ratio of faults is computed by taking the ratio between the magnitudes of their two principle components (i.e., Eigenvalues).

3.1.2. Inverting for Geometry

With a parameterized geometry, it is possible to invert for the unknown structure of the diapir with the help of an observable. Using a scaling parameter set of 1.2, 2.0, 0.8, 0.6 ($S_1 - S_4$), and 0.94 (Sz), we produce a synthetic diapir (blue in Figure 3) similar to the interpretation of Jones and Davison (2014). We then forward model the evolution of this diapir in an extensional setting for 100 kyrs which results in a single normal fault (Figure 4a). The size, location and orientation of that fault might be visible in a seismic study (Juhlin et al., 2010) and could serve as an observable which we can use to constrain the diapir geometry through inversion.

We compare the faults developed by the 1,500 variations to our synthetic observation (fault in Figure 4a, developed by the blue diapir in Figure 3). After identifying the 50 best fitting models, we create 8 new variations with similar parameters for each one to improve our coverage in the area of low misfit (Sambridge, 1999, Neighborhood algorithm). This procedure is commonly used to deal with non-linear and -unique inverse problems (e.g., Baumann & Kaus, 2015) and is repeated four times here, yielding a final ensemble of about 3,100 variations. After 2 iterations, it was clear that the minimum for Sx_4 was close to our initial lower bound of 0.5 (Table S3 in Supporting Information S1) and we relaxed the bound to 0.25 for the third and fourth iteration of the neighborhood algorithm.

We also perform a second inversion, using only 2 control polygons (locations are shown in Figure 6) alongside vertical scaling to investigate how robust the approach is. Because of the smaller parameter space, we test an initial set of about 500 variations and then add 4×400 variations with the neighborhood algorithm for the 2 control polygon case.

Computing a misfit between two geometric observations is not as straight forward as comparing numeric outputs and observations. To address this issue, Wijns et al. (2003) used human appraisal to rank modeled faulting patterns, while Boschetti et al. (2003) utilized self organizing maps to do the same. We compute the misfit of an individual fault pattern, by combining some of the geometric properties of the modeled fault and comparing them to our synthetic observation:

$$\Phi_i = \left(\frac{\sqrt{(|x_i| - |x_o|)^2 + (z_i - z_o)^2}}{l_n} + \frac{||\alpha_i| - |\alpha_o||}{\alpha_n} + \frac{|r_i - r_o|}{r_n} \right) \times N \quad (4)$$

Φ_i is the misfit of a fault to our synthetic observation. Subscript $_i$ corresponds to the geometry variation, subscript $_o$ to the synthetic observation and subscript $_n$ to a normalization constant for each property. The first term of the right hand side compares the location of the fault centers with x corresponding to the lateral and z to the vertical coordinate. α is the angle between the fault and the horizontal direction and r the aspect ratio of the fault. N is the number of faults that develop. l_n is 2 km, a tenth of the model width, α_n is 5° and $r_n = r_o$. These parameters were chosen to make sure that all three right hand side terms are in the range of 0–1 for the majority of models. Figure 4 shows how large each of the three terms of Equation 4 are for 8 selected fault systems.

We decided to use the absolute values of x and α as Section 4.1.1 suggests that the side, to which the faults develop, is not coupled to the geometry but is related to how the curved diapir boundaries intersect with the rectangular grid. This is supported by the fact that the issue persists at higher resolution models and disappears for the asymmetric cases (Text S4 and Figure S8 in Supporting Information S1).

3.2. Application II: Subduction

We use the method introduced in Section 2.3 to test the dependence of plate velocity on the initial dip angle (β_0) of the subducting slab. Using a reference model, dipping with 60°, we test 16 variations in the range of 30°–90°. We use a simple 2D model with an oceanic plate of 70 km thickness (corresponding to a thermal age of 30 Myr) subducting underneath a continent of 100 km thickness. Both plates are free (i.e., not fixed to the edges of the model) and as we do not prescribe any boundary velocities, the movement of the plates is entirely driven by the negative buoyancy of the cold slab. We test models with a 20 km (4 cells) and 30 km (6 cells) wide weak zone. Text S3 in Supporting Information S1 provides more details on the setup and the thermomechanical code we use.

4. Results

4.1. Application I: Salt

4.1.1. Faulting Patterns in Dependence of Initial Geometry

To accommodate the extension, the models start developing faults at the tip of the diapir as well as the surface. The faults then grow from the surface downwards or from the diapir upwards and eventually connect both (Figure S6 in Supporting Information S1). In the majority of cases, the strain then focuses on one of the two directions and a single fault forms, taking up most of the deformation. Both sides were preferred in a large number of models for all heights of diapirs (Figures 4b and 4c). In about 25% of the cases, the fault did not connect to the center of the diapir, but instead it formed at the edges of the diapir top (Figures 4d–4h). For some tall diapirs, the deformation did not focus on a single fault but was distributed over an area close to the surface (Figure 4e). In some cases, one dominant fault formed, but a part of the deformation was also accommodated by other parallel and opposite faults (Figures 4g and 4h). In few cases, two faults formed that shared the strain between them (Figures 4f and 4i).

Figure 5 shows a selection of geometric fault properties in dependence of the scaling parameters applied to the diapir. Figure S7 in Supporting Information S1 shows all relations between scaling parameters and fault properties. Intuitively, there is a good correlation between the height of diapir (Sz) and the depth of the lower end of the fault as the fault connects the top of the diapir to the surface (Figure 5a). It is, however, evident that there is some spread toward deeper fault tips as well. This deviation represents cases where the fault does not start at the tip or center of the diapir, but instead to one of the sides (Figures 4d–4h). We use the relation between Sz and the depth of the fault tip to discriminate between faults that connect to the center of the diapir (blue in Figure 5) and faults that connect to the sides (orange).

The aspect ratio scales similarly with Sz as the depth of the fault tip because long faults are not wider than short faults (Figure 5b). The spread is a bit bigger and there are more anomalous cases. Where Sz and r are small, two crossing faults developed (Figure 4i) and the image processing was not able to properly split them, returning flawed values for the width. Cases of low r and large Sz relate to those shown in Figures 4e and 4h and predominantly happen when the faults do not form in the center of the diapir (orange in Figure 5b).

Figure 5c shows that most faults have an angle of roughly 50°. It also shows a striking dependence of the fault location on S_2 (the neck of the diapir). For small S_2, the faults form almost exclusively to the sides of the diapir (orange) while they occur predominantly in the center (blue) for high S_2. Overall, more faults extend to the right. Given that the diapirs are symmetric, this may be due to small asymmetries that arise from gridding.

Figure 5d relates the width of the diapir head (S_4) and the lateral coordinate of the fault center. It shows that the faults form further from the center of the domain, the wider the diapir is. This is the only correlation for S_4 (Figure S7 in Supporting Information S1). The figure also clearly shows the two different trends of faults forming in the

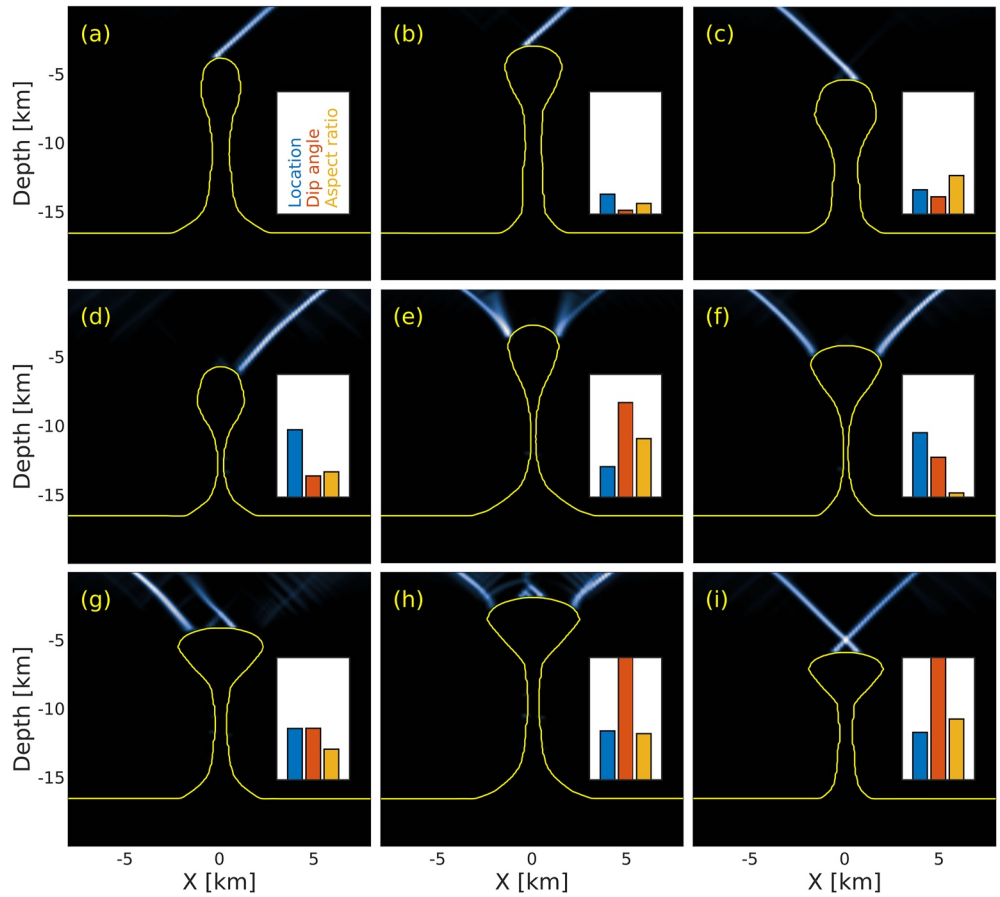

Figure 4. Accumulated plastic strain after 100 kyrs corresponding to normal faults that formed to accommodate the extension of the model. (a) Synthetic "true" diapir (blue in Figure 3) and corresponding fault which serves as our synthetic observation, other faults are compared to (Equation 4). (b, c) "Regular case": Deformation focuses on a single fault for different diapir heights. This happens for the majority of cases. (d) Deformation focuses on a single fault but the fault does not start at the center of the diapir top. (e) Deformation is not taken up by a single fault but two areas with a lot of small faults. (f) Faults form on both sides of the diapir. (g) Two parallel faults form with some minor opposite ones. (h) A large number of smaller faults develop. (i) Model develops two crossing faults. Insets show misfit of the observed fault/fault system to the synthetic observation in (a). Blue bar corresponds to the location term, orange to the orientation term and yellow to the aspect ratio term of Equation 4.

center or at the sides of the diapir head with few exceptions. S_1 (width of the diapir base) and S_3 (width at transition zone from neck to head of the diapir) do not show any correlation with any of the faults' geometric properties (Figure S7 in Supporting Information S1).

We also tested two sets of models with the same scaling parameters but a slightly asymmetric reference model (red dotted and red dashed-dotted in Figure 3). The results are presented in Text S4 and Figure S8 in Supporting Information S1.

4.1.2. Inverting for Geometry

After four iterations of the neighborhood algorithm, we have a total of 3,100 models. Figure 6a shows the 200 diapirs that develop faults with the lowest misfit in comparison with the synthetic observation (fault in Figure 4a). All 200 are almost a perfect match for the head of the diapir in terms of height and shape. The transition between head and neck of the diapir shows very large spread over almost the entire range of possible extents. The neck and base of diapir show less spread but are not as well constrained compared as the top of the diapir.

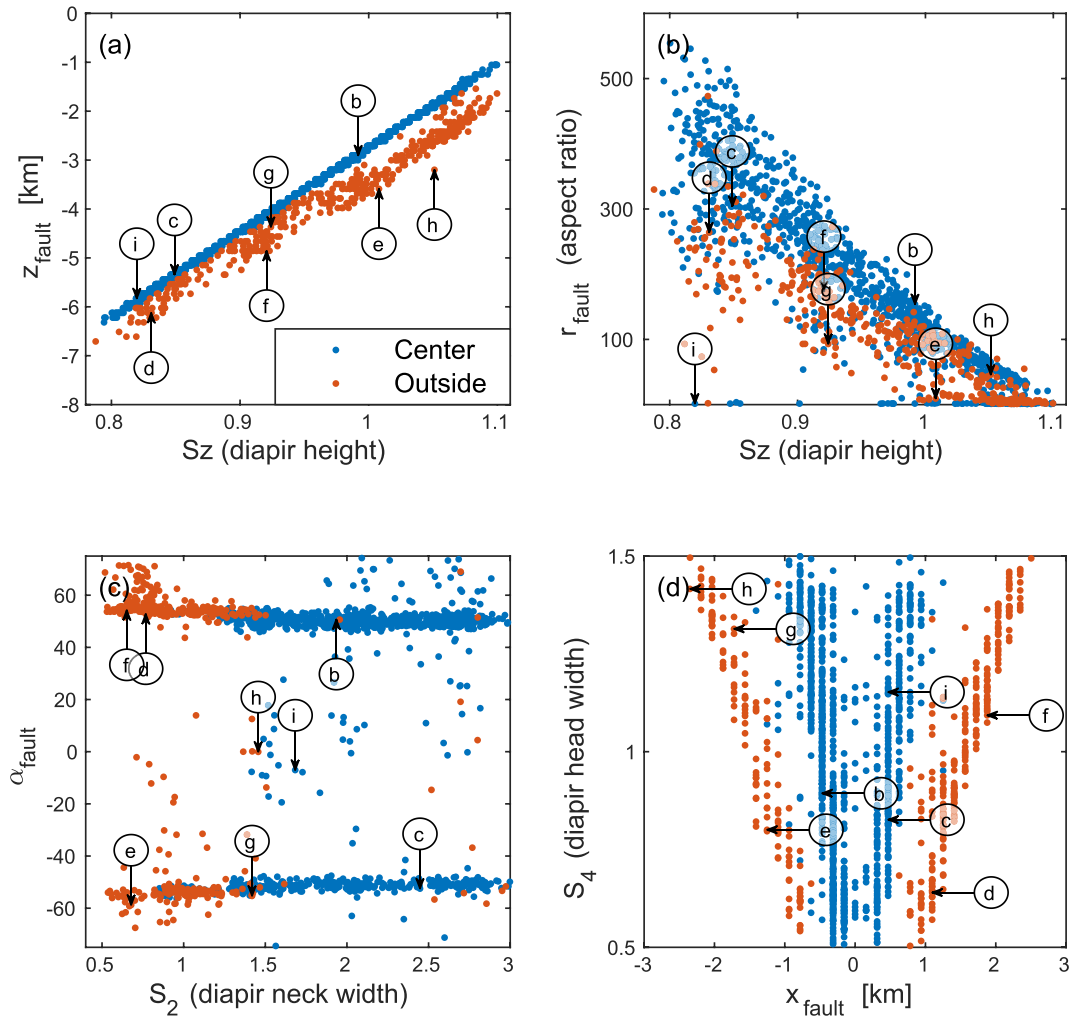

Figure 5. Different fault properties (α, r, x, z) in relation to scaling parameters. Arrows show where the examples in Figures 4b–4i plot to relate fault types with the parameters. (a) Depth of the lower end of the fault in dependence of Sz. This allows for the distinction between faults that start from the center (blue) and faults that start from at the side (orange) of the diapir. Same color code in b–d. (b) Fault aspect ratio in dependence of Sz. (c) Fault orientation in dependence of S_2. $\alpha < 0$: fault goes to the left. (d) Lateral position of the fault center in dependence of S_4.

Figure 6b shows the misfit of each model in dependence of the two most important parameters, the width of the diapir head (S_4) and the height of the diapir (Sz). Sz is the most well defined parameter with models outside the range of 0.9–1.0 showing large misfit. But inside that range, there is also a correlation between misfit and S_4 with the minimum in the area of 0.6. As the location of this minimum is very close to our lower bound for Sx_4, we extended it from 0.5 to 0.25 for the last 2 iterations of the neighborhood algorithm.

Figures 6c and 6d show the results of attempting the same inversion by only using 2 control polygons instead of 4 alongside vertical scaling to fit the synthetic observation. Again, the height and upper part of the head as well as the thickness of the diapir neck are well constrained. Most low-misfit geometries have a kink at 7 km depth which is the result of fitting both the shape of the head and width of the neck with only 2 control polygons. Furthermore, none of the low-misfit models have the correct width of the diapir base.

4.2. Application II: Subduction

All subduction models start out with an initial stage of slab rollback, trench retreat and continent extension while the slab starts sinking. Over time, the horizontal velocity of the suducting plate increases depending on the angle of the slab (Figure 7). Models that start with a steep subduction angle ($\beta_0 > 65°$) eventually reach a stage where

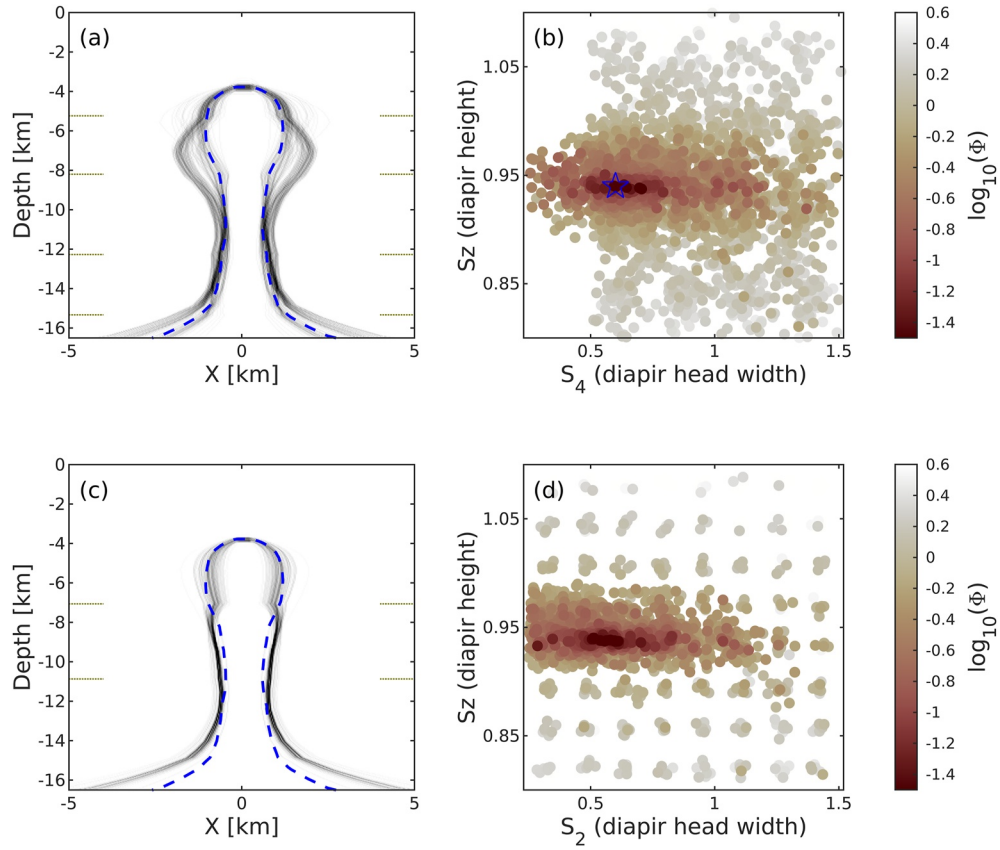

Figure 6. (a) Synthetic diapir in dashed blue (solid blue in Figure 3) and the 200 variations out of 3,100 with the smallest misfit in gray. Dots on the sides indicate locations of the 4 control polygons. (b) Misfit ($\log_{10}(\Phi)$) as a function of width of the diapir head (S_4) and height of the diapir (Sz). Note the denser distribution of samples around the minimum courtesy of the neighborhood algorithm. Blue star indicates the location of the synthetic "true" geometry (dashed blue in (a)). Figure S9 in Supporting Information S1 shows misfit as a function of all parameter combinations. (c) Similarly to (a), Top 200 out of 2,100 variations, using 2 control polygons. (d) Misfit as function of diapir height and head width for the 2 control polygon example.

velocities increase strongly and the trench reverses direction and starts to advance toward the continent, leading to shortening of the fore-arc. Once the slab approaches the bottom of the model, velocities decrease again. This also stops the advance of the trench, leading to another rollback period.

4.2.1. Convergence Velocity

In Figure 8a, we show the difference between the average horizontal velocities of subducting and overriding plate (i.e., the convergence velocity) as a function of time and initial subduction angle β_0. Within the first 2 Myr, all models undergo a period of convergence with maximum velocities of 4 cm yr^{-1} for low β_0 and 7 cm yr^{-1} for high β_0. In this period, the convergence velocity is mainly caused by the retreat of the trench (see also Figure 7). For $\beta_0 <= 65°$, the convergence rate then slowly declines over time. However, models that start with a steeper slab go through a second period of rapid acceleration after about 4 Myr, reaching up to 9 cm yr^{-1} at $\beta_0 = 80°$ before declining as well. In this period, the velocity of the subducting plate is the main contributor to the convergence velocity (Figure 7). While velocities generally increase with β_0, they drastically decrease again at $\beta_0 > 85°$ as we approach a vertical initial slab. Text S5 in Supporting Information S1 presents an example of how a velocity profile (e.g., Sdrolias & Müller, 2006) can be used to invert for the initial subduction angle β_0 similar to Section 4.1.2.

Models with a wider weak zone (30 km instead of 20 km) show the same general behavior, but the velocity of both plates is higher. There are also more models that enter the second phase of acceleration (Figure 7).

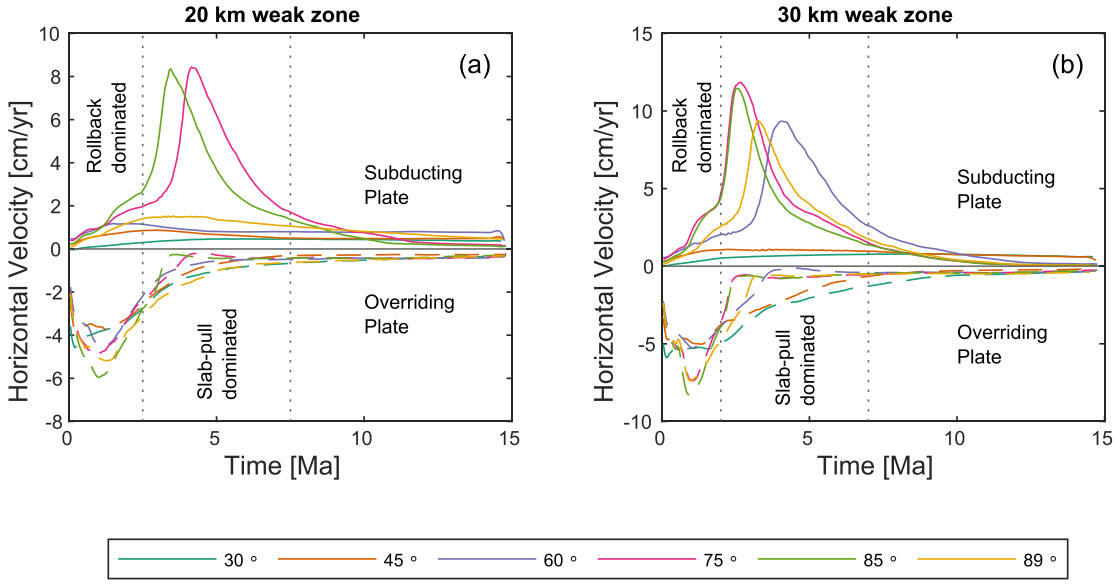

Figure 7. Average velocity of subducting (solid lines in upper panel) and overriding plate (dashed lines in lower panel) in dependence of time for a selection of different initial slab angles (β_0). Dotted vertical lines indicate periods dominated by different mechanisms. Within the first 2.5 Myr, the convergence is mostly accommodated by slab rollback and trench retreat. In the following 5 Myr, it is dominated by the trenchward motion of the subducting plate. (a) Models have a weak zone that is 20 km wide (about 4 grid cells). (b) Models have a weak zone 30 km wide (about 6 grid cells).

4.2.2. Subduction Angle

Figure 8b shows the evolution of the dip angle for all models. While slabs that start out with a shallow dip angle gradually steepen over time, slabs that start steep quickly undergo flattening until leveling out at about 60°. Models that undergo a second phase of acceleration (see Figure 8a) slightly steepen from 55° to 65° during that period again. Once the slabs start approaching the bottom of the model (660 km depth), they flatten toward 45°. All models converge to a dip angle between 45° and 55° which is agreement with global averages as reported by Lallemand et al. (2005) and Syracuse and Abers (2006).

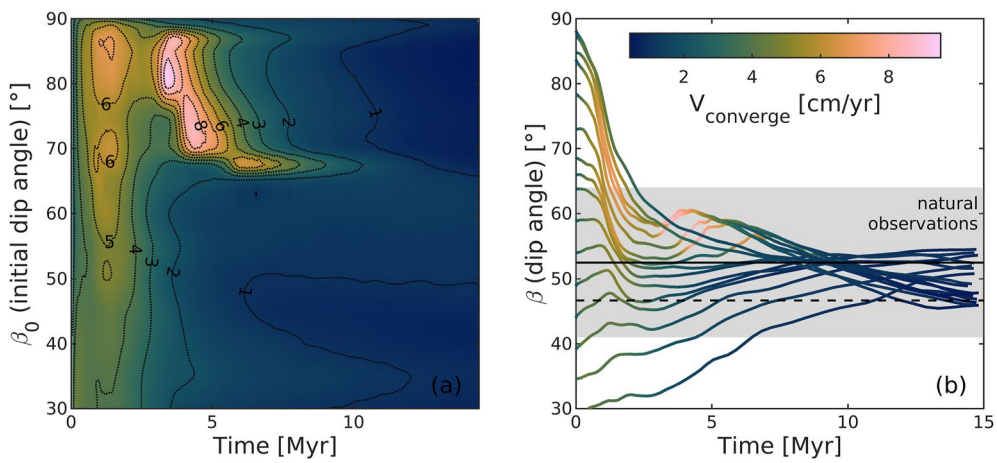

Figure 8. (a) Convergence rate between oceanic and continental plate in dependence of initial subduction angle (β_0) through time. (b) Dip angle of the subducting slab (β) as a function of time for all models. Color gradient along the curves shows convergence velocity. Solid black line shows global average of dip angles from Lallemand et al. (2005) and shaded gray area indicates one standard deviation. Dashed black line shows global average of dip angles from Syracuse and Abers (2006).

5. Discussion

5.1. Parameterization and Transformation

The method we present in this study is based on two main concepts. The use of a reference geometry (sphere in Section 2.2 and Figure 1, red plate in Section 2.3 and Figure 2, red outline in Section 3.1 and Figure 3, $\beta_0 = 60°$ model in Section 3.2) and control polygons/rotation centers that act as anchors for the transformation.

5.1.1. Strengths and Weaknesses

Using a reference geometry removes the necessity to define a large number of coordinates for every new variation. Instead, each complex shape is represented by a small number of values that describe how it is different to the reference geometry. This comes at the price of limiting the shape of possible variations. It would for instance not be possible to make the diapir in Figure 3 lean toward one side, introduce any asymmetry (in the x-y-plane) that was not present before or split the head in two without creating a new reference model with those features. But since the initial geometry of geodynamic models is commonly constrained by imaging surveys, there usually is enough information to create an appropriate reference model of the geological unit (Figure 3).

The use of control polygons and interpolation between them allows us to greatly reduce the number of necessary parameters compared to providing scaling parameters for each polygon or changing individual coordinates/vertices. Homogeneous three-dimensional scaling of the body is possible with a single control polygon and parameter ($Sx = Sy = Sz$). At the same time, complex changes as shown in Figure 1 can be achieved with only 6 or 7 parameters. Free choice of the position of the control polygons allows for great flexibility. The closer control polygons are to another, the shorter the wavelength of variation. If a part of the geological unit is well constrained, this part can be kept locked by bounding it with two control polygons with constant scaling parameters of 1, while the other parts can stay variable. As mentioned before, our transformations cannot introduce additional complexity into the individual polygons.

Figure 6c illustrates that using a smaller number of control polygons (2 instead of 4) can be sufficient to fit the most influential features of the diapir. But it also demonstrates a potential pitfall of using few control polygons. Because the observation (fault system) is sensitive to the neck width but not the base width (Figures 6a and S7 in Supporting Information S1) but both features are governed by the same control polygon, the base of the diapir appears to be well constrained but is actually wrong (Figure 6c). It is important to keep in mind that each control polygon should only govern one feature of a body.

5.1.2. Relation to Other Approaches

Our approach shares similarities with that of Sevilla et al. (2020) which also applies 2D transformations at different levels of the third dimension that control how the entire 3D shape is transformed. Both methods seem capable of producing similar transformations with the same number of parameters but we consider the scaling parameters to be more intuitive than the control points of NURBS surfaces.

There is also similarity to the work of Galley et al. (2020) as groups of surface nodes are moved together to preserve smooth surfaces while other groups of nodes remain stationary. In the case of the diapir (Figure 3) we can change height and width at 4 levels with only 5 parameters whereas moving a single surface vertex in 2D already requires 2 parameters. The approach of Galley et al. (2020) does in turn provide more flexibility to introduce asymmetric features.

Our adaptation for subduction zones shares the philosophy of using a combination of arbitrary coordinates (provided by the Inkscape drawing) and features that are specific to subduction zones like dip angle and plate thickness with the GWB (Fraters et al., 2019). The main difference is the use of a reference geometry which means that weak zone, crust and flattening/steepening segments can be added with one or two parameters each instead of building the plate out of individual segments each requiring three or more parameters. By not relying on a reference geometry, the GWB has advantages in quickly introducing big geometry changes.

5.2. Importance of Initial Geometry

Both applications (more details in the following sections) demonstrate that different initial geometries within the range of uncertainty of geophysical imaging can lead to drastically different modeling results. Therefore, it is

crucial to test different setups and develop an understanding of the influence that the geometry of the geological structures can have. While this finding is not necessarily new as previous studies have highlighted the dependence of results on initial geometry (e.g., Duretz et al., 2020; Le Pourhiet et al., 2003), the issue often remains unaddressed in many state-of-the-art geodynamic studies (see Section 1) that use a single geometry or a handful of end-member cases without parameterization (e.g., Liao et al., 2017; Tetreault & Buiter, 2012).

Our approach enables the user to quickly, on the order of a second per version, and automatically create any number of variations of a complex 3D body in their model. This not only allows for the incorporation of uncertain constraints but can also reveal unexpected dependencies of the model results on the initial geometry of the model. The scaling parameters even facilitate a quantitative description of such dependencies.

5.3. Application to Salt

Figure 4 shows how different initial salt geometries result in distinctly different faults. We observe some intuitive relationships like the link between height of the diapir and position or aspect ratio of the fault (Figures 5a and 5b). But, we also find unexpected correlations like a thin diapir neck facilitating faults at the sides of the diapir (Figure 5c). We also learn that the base of the diapir (S_1) and the transition from head to neck (S_3) have little to no impact on the developing faults and could therefore be kept constant in further investigations of the system.

It is apparent that faults can develop to both sides of the diapir independently of the geometry for the symmetric case. For the asymmetric case, faults that develop at the side of the diapir head exclusively appear on the side that has a stronger curvature (Figures S8c and S8f in Supporting Information S1). We tested the asymmetry on both sides to exclude the possibility that this effect is caused by our grid discretization.

Finally, we can see that, given the observation of a fault and a good understanding of the material parameters, geodynamic modeling could help improve imaging results and reduce ambiguity regarding the extent of a diapir. Figure 6 shows that it is in principle possible to constrain the height and head width of the diapir with the help of an observed fault while deeper structures that have no influence on the faulting pattern remain blurred. Applying this to a natural example would involve more unknowns like the material parameters of salt and crust, additional crustal layers, heterogeneities in the salt and topography, resulting in a larger parameter space to consider. However, geometry, parameterized by scaling parameters, can be included in such a study (Spang et al., 2021).

5.4. Application to Subduction

Figures 7 and 8a show how strongly the velocity of plates and the entire dynamics of the model depend on the initial angle of the subducting slab. While models with an initial angle $\beta_0 <= 65°$ move at relatively even velocities throughout 15 Myr, models with steeper slabs run through a period of strongly increasing velocities that are high enough to stop or even reverse the retreat of the trench. The timing and maximum velocity of this phase of acceleration also depend on the initial geometry of the model.

Another geometrical parameter that strongly influences the velocities of the plates is the thickness of the weak zone between subducting and overriding plate (Figure 7). With a thicker weak zone, there is less friction between the plates and they reach higher velocities. So, both parameters (initial dip angle of the slab and thickness of the weak zone) can exert a first order control on the model dynamics and could overprint a lot of other effects. With our method, it is easy to change either parameter and investigate their influence on the model results without investing a lot of time into creating different initial geometries.

Figure 8b shows that independently from the initial subduction angle (β_0), all models converge to a similar angle of about 50° after a few Myr. This range is in agreement with global averages of subucting slabs (Lallemand et al., 2005; Syracuse & Abers, 2006) which suggests that 50° is the preferred angle for long-term slab-pull-dominated subduction.

6. Conclusion

In this study, we present a simple and intuitive method to describe and manipulate 3D bodies in a heterogeneous manner with a limited set of parameters. This not only allows us to include uncertainties about initial geometry in the modeling process, but also enables us to quantify the relationship between initial geometry of a model and

the computed output. As shown by our study and Spang et al. (2021), this allows us to even improve constraints on geometry by integrating different observations and invert for geometric properties.

We present two application examples. (a) A salt diapir with an ambiguous geometry in seismic imaging. We show that slight geometric variations that would all satisfy the imaging data, can result in the development of vastly different faulting patterns in an extending regime. It is also evident that small asymmetries in the diapir lead to distinctive differences in the developing faults around the diapir. Furthermore, we show that, with our parameterization, initial geometry can be treated like any material parameter and included in sensitivity studies or inversion frameworks. (b) A subduction zone where we vary the initial dip angle of the subducting slab as well as the thickness of the weak zone between subducting and overriding plate. Both parameters influence the velocity evolution of the plates by an order of magnitude. We show that, independently of the initial dip angle, all slabs approach a subduction angle of about 50°.

Our study presents an intuitive method to parameterize and manipulate the initial geometry of geodynamic models and highlights the importance of considering different geometries instead of using just one. We implemented the method as a tool in the open-source software package geomIO which is fully compatible with the open-source, thermomechanical stokes code LaMEM. Areas of application include salt tectonics, subduction settings, volcanic systems with varying sizes/shapes of magma bodies and models of orogenesis with uncertain extents of critical units. As geomIO can forward model Bouguer anomalies, constraints from gravity surveys can directly be considered in the creation of the initial geometry of geodynamic models.

Data Availability Statement

Software used for this research is available on zenodo at: https://doi.org/10.5281/zenodo.6538270 (Bauville & Baumann, 2019; Kaus et al., 2016).

Acknowledgments
The authors thank John Naliboff, Florian Wellmann and one anonymous reviewer for their help in improving the quality of the manuscript. This study was funded by the European Research Council through the MAGMA project, ERC Consolidator Grant # 771143. We used perceptually uniform colormaps to prevent optical data distortion (Crameri, 2018). Parts of this research were conducted using the supercomputer Mogon II and/or advisory services offered by Johannes Gutenberg University Mainz (hpc.uni-mainz.de), which is a member of the AHRP (Alliance for High Performance Computing in Rhineland Palatinate, www.ahrp.info) and the Gauss Alliance e.V. Open Access funding enabled and organized by Projekt DEAL.

References

Alisic, L., Gurnis, M., Stadler, G., Burstedde, C., Wilcox, L. C., & Ghattas, O. (2010). Slab stress and strain rate as constraints on global mantle flow. Geophysical Research Letters, *37*(22). https://doi.org/10.1029/2010gl045312

Baumann, T. S., & Kaus, B. J. P. (2015). Geodynamic inversion to constrain the non-linear rheology of the lithosphere. *Geophysical Journal International*, *202*(2), 1289–1316. https://doi.org/10.1093/gji/ggv201

Baumann, T. S., Kaus, B. J. P., & Popov, A. A. (2014). Constraining effective rheology through parallel joint geodynamic inversion. *Tectonophysics*, *631*, 197–211. https://doi.org/10.1016/j.tecto.2014.04.037

Bauville, A., & Baumann, T. S. (2019). geomIO: An open-source MATLAB toolbox to create the initial configuration of 2-D/3-D thermo-mechanical simulations from 2-D vector drawings. *Geochemistry, Geophysics, Geosystems*, *20*(3), 1665–1675. https://doi.org/10.1029/2018GC008057

Beucher, R., Moresi, L., Giordani, J., Mansour, J., Sandiford, D., Farrington, R., et al. (2019). UWGeodynamics: A teaching and research tool for numerical geodynamic modelling. *Journal of Open Source Software*, *4*(36), 1136. https://doi.org/10.21105/joss.01136

Bosch, M., Mukerji, T., & Gonzalez, E. F. (2010). Seismic inversion for reservoir properties combining statistical rock physics and geostatistics: A review. *Geophysics*, *75*(5), 75A165–75A176. https://doi.org/10.1190/1.3478209

Boschetti, F., Wijns, C., & Moresi, L. (2003). Effective exploration and visualization of geological parameter space. *Geochemistry, Geophysics, Geosystems*, *4*(10), 1086. https://doi.org/10.1029/2002gc000503

Caumon, G., Collon-Drouaillet, P., Le Carlier de Veslud, C., Viseur, S., & Sausse, J. (2009). Surface-based 3D modeling of geological structures. *Mathematical Geosciences*, *41*(8), 927–945. https://doi.org/10.1007/s11004-009-9244-2

Čížková, H., & Bina, C. R. (2015). Geodynamics of trench advance: Insights from a Philippine-Sea-style geometry. *Earth and Planetary Science Letters*, *430*, 408–415. https://doi.org/10.1016/j.epsl.2015.07.004

Crameri, F. (2018). Scientific colour-maps. Zenodo, *10*. https://doi.org/10.5281/zenodo.1243862

Duretz, T., Asti, R., Lagabrielle, Y., Brun, J.-P., Jourdon, A., Clerc, C., & Corre, B. (2020). Numerical modelling of Cretaceous Pyrenean Rifting: The interaction between mantle exhumation and syn-rift salt tectonics. *Basin Research*, *32*(4), 652–667. https://doi.org/10.1111/bre.12389

Frank, T., Tertois, A.-L., & Mallet, J.-L. (2007). 3D-reconstruction of complex geological interfaces from irregularly distributed and noisy point data. *Computers & Geosciences*, *33*(7), 932–943. https://doi.org/10.1016/j.cageo.2006.11.014

Fraters, M., Thieulot, C., Van Den Berg, A., & Spakman, W. (2019). The geodynamic World builder: A solution for complex initial conditions in numerical modeling. *Solid Earth*, *10*(5), 1785–1807. https://doi.org/10.5194/se-10-1785-2019

Fullagar, P. K., Hughes, N. A., & Paine, J. (2000). Drilling-constrained 3D gravity interpretation. *Exploration Geophysics*, *31*(2), 17–23. https://doi.org/10.1071/eg00017

Galley, C. G., Lelièvre, P. G., & Farquharson, C. G. (2020). Geophysical inversion for 3d contact surface geometry. *Geophysics*, *85*(6), K27–K45. https://doi.org/10.1190/geo2019-0614.1

Guillen, A., Courrioux, G., Calcagno, P., Lane, R., Lees, T., Mclnerney, P., & McInerney, P. (2004). Constrained gravity 3D litho-inversion applied to Broken Hill. *ASEG Extended Abstracts*, *2004*(1), 1–6. https://doi.org/10.1071/aseg2004ab057

Jackson, C. A.-L., & Lewis, M. M. (2012). Origin of an anhydrite sheath encircling a salt diapir and implications for the seismic imaging of steep-sided salt structures, Egersund Basin, Northern North Sea. *Journal of the Geological Society*, *169*(5), 593–599. https://doi.org/10.1144/0016-76492011-126

Jadamec, M. A., Billen, M. I., & Roeske, S. M. (2013). Three-dimensional numerical models of flat slab subduction and the Denali fault driving deformation in south-central Alaska. *Earth and Planetary Science Letters*, *376*, 29–42. https://doi.org/10.1016/j.epsl.2013.06.009

Jessell, M. (2001). Three-dimensional geological modelling of potential-field data. *Computers & Geosciences*, *27*(4), 455–465. https://doi.org/10.1016/s0098-3004(00)00142-4

Jones, I. F., & Davison, I. (2014). Seismic imaging in and around salt bodies. *Interpretation*, *2*(4), SL1–SL20. https://doi.org/10.1190/INT-2014-0033.1

Juhlin, C., Dehghannejad, M., Lund, B., Malehmir, A., & Pratt, G. (2010). Reflection seismic imaging of the end-glacial Pärvie Fault system, northern Sweden. *Journal of Applied Geophysics*, *70*(4), 307–316. https://doi.org/10.1016/j.jappgeo.2009.06.004

Kaus, B. J. P., Popov, A. A., Baumann, T., Pusok, A., Bauville, A., Fernandez, N., & Collignon, M. (2016). Forward and inverse modelling of lithospheric deformation on geological timescales. In *Proceedings of NIC symposium*.

Lallemand, S., Heuret, A., & Boutelier, D. (2005). On the relationships between slab dip, back-arc stress, upper plate absolute motion, and crustal nature in subduction zones. *Geochemistry, Geophysics, Geosystems*, *6*(9), Q09006. https://doi.org/10.1029/2005gc000917

Le Pourhiet, L., Burov, E., & Moretti, I. (2003). Initial crustal thickness geometry controls on the extension in a back arc domain: Case of the Gulf of Corinth. *Tectonics*, *22*(4), 1032. https://doi.org/10.1029/2002tc001433

Liao, J., Gerya, T., Thielmann, M., Webb, A. A. G., Kufner, S.-K., & Yin, A. (2017). 3D geodynamic models for the development of opposing continental subduction zones: The Hindu Kush–Pamir example. *Earth and Planetary Science Letters*, *480*, 133–146. https://doi.org/10.1016/j.epsl.2017.10.005

Moresi, L., Dufour, F., & Mühlhaus, H.-B. (2002). Mantle convection modeling with viscoelastic/brittle lithosphere: Numerical methodology and plate tectonic modeling. *Pure and Applied Geophysics*, *159*(10), 2335–2356. https://doi.org/10.1007/s00024-002-8738-3

Oldenburg, D., & Pratt, D. (2007). Geophysical inversion for mineral exploration: A decade of progress in theory and practice. *Proceedings of exploration*, *7*, 61–95.

Pearse, J., & Fialko, Y. (2010). Mechanics of active magmatic intraplating in the Rio Grande Rift near Socorro, New Mexico. *Journal of Geophysical Research*, *115*(B7), B07413. https://doi.org/10.1029/2009jb006592

Pereyra, V. (1996). Modeling, ray tracing, and block nonlinear travel-time inversion in 3D. *Pure and Applied Geophysics*, *148*(3), 345–386. https://doi.org/10.1007/bf00874572

Ratnaswamy, V., Stadler, G., & Gurnis, M. (2015). Adjoint-based estimation of plate coupling in a non-linear mantle flow model: Theory and examples. *Geophysical Journal International*, *202*(2), 768–786. https://doi.org/10.1093/gji/ggv166

Reuber, G. S., Kaus, B. J. P., Popov, A. A., & Baumann, T. S. (2018). Unraveling the physics of the Yellowstone magmatic system using geodynamic simulations. *Frontiers of Earth Science*, *6*, 117. https://doi.org/10.3389/feart.2018.00117

Sambridge, M. (1999). Geophysical inversion with a neighbourhood algorithm-I. Searching a parameter space. *Geophysical Journal International*, *138*(2), 479–494. https://doi.org/10.1046/j.1365-246X.1999.00876.x

Schaaf, A., de la Varga, M., Wellmann, F., & Bond, C. E. (2021). Constraining stochastic 3-D structural geological models with topology information using approximate Bayesian computation in GemPy 2.1. *Geoscientific Model Development*, *14*(6), 3899–3913. https://doi.org/10.5194/gmd-14-3899-2021

Sdrolias, M., & Müller, R. D. (2006). Controls on back-arc basin formation. *Geochemistry, Geophysics, Geosystems*, *7*(4), Q04016. https://doi.org/10.1029/2005gc001090

Sevilla, R., Zlotnik, S., & Huerta, A. (2020). Solution of geometrically parametrised problems within a cad environment via model order reduction. *Computer Methods in Applied Mechanics and Engineering*, *358*, 112631. https://doi.org/10.1016/j.cma.2019.112631

Spang, A., Baumann, T., & Kaus, B. (2021). A multiphysics approach to constrain the dynamics of the Altiplano-Puna magmatic system. *Journal of Geophysical Research: Solid Earth*, *126*(7), e2021JB021725. https://doi.org/10.1029/2021jb021725

Syracuse, E. M., & Abers, G. A. (2006). Global compilation of variations in slab depth beneath arc volcanoes and implications. *Geochemistry, Geophysics, Geosystems*, *7*(5), Q05017. https://doi.org/10.1029/2005gc001045

Tetreault, J. á., & Buiter, S. (2012). Geodynamic models of terrane accretion: Testing the fate of island arcs, oceanic plateaus, and continental fragments in subduction zones. *Journal of Geophysical Research*, *117*(B8), B08403. https://doi.org/10.1029/2012jb009316

van Zelst, I., Crameri, F., Pusok, A. E., Glerum, A., Dannberg, J., & Thieulot, C. (2021). 101 Geodynamic modelling: How to design, carry out, and interpret numerical studies. Solid Earth Discussions, 1–80.

Varga, M. D. L., Schaaf, A., & Wellmann, F. (2019). GemPy 1.0: Open-source stochastic geological modeling and inversion. *Geoscientific Model Development*, *12*(1), 1–32. https://doi.org/10.5194/gmd-12-1-2019

Wellmann, F., & Caumon, G. (2018). 3-D Structural geological models: Concepts, methods, and uncertainties. *Advances in Geophysics*, *59*, 1–121.

Wijns, C., Boschetti, F., & Moresi, L. (2003). Inverse modelling in geology by interactive evolutionary computation. *Journal of Structural Geology*, *25*(10), 1615–1621. https://doi.org/10.1016/s0191-8141(03)00010-5

References From the Supporting Information

Baumann, T. S., Kaus, B., & Popov, A. A. (2018). Deformation and stresses related to the gorleben salt structure: Insights from 3D numerical models. *Mechanical Behavior of Salt, Saltmech*, *IX*, 15–27.

Crameri, F., Schmeling, H., Golabek, G. J., Duretz, T., Orendt, R., Buiter, S., et al. (2012). A comparison of numerical surface topography calculations in geodynamic modelling: An evaluation of the 'sticky air' method. *Geophysical Journal International*, *189*(1), 38–54. https://doi.org/10.1111/j.1365-246x.2012.05388.x

Drucker, D. C., & Prager, W. (1952). Soil mechanics and plastic analysis or limit design. *Quarterly of Applied Mathematics*, *10*(2), 157–165. https://doi.org/10.1090/qam/48291

Harlow, F. H., & Welch, J. E. (1965). Numerical calculation of time-dependent viscous incompressible flow of fluid with free surface. *Physics of Fluids*, *8*(12), 2182–2189. https://doi.org/10.1063/1.1761178

Ingraham, M. D., Broome, S. T., Bauer, S. J., Barrow, P. C., & Flint, G. M. (2015). Behavior of salt from the Bayou Choctaw salt dome. In *49th US Rock Mechanics/Geomechanics Symposium*.

Kaus, B. J. P., Mühlhaus, H., & May, D. A. (2010). A stabilization algorithm for geodynamic numerical simulations with a free surface. *Physics of the Earth and Planetary Interiors*, *181*(1–2), 12–20. https://doi.org/10.1016/j.pepi.2010.04.007

Martinod, J., Husson, L., Roperch, P., Guillaume, B., & Espurt, N. (2010). Horizontal subduction zones, convergence velocity and the building of the Andes. *Earth and Planetary Science Letters*, *299*(3–4), 299–309. https://doi.org/10.1016/j.epsl.2010.09.010

Zong, J., Stewart, R. R., Dyaur, N., & Myers, M. T. (2017). Elastic properties of rock salt: Laboratory measurements and Gulf of Mexico well-log analysis. *Geophysics*, *82*(5), D303–D317. https://doi.org/10.1190/geo2016-0527.1